Plastic strain-induced sequential martensitic transformation

Shaolou Wei [a], Jinwoo Kim [a], Jaclyn Leigh Cann [a], Reza Gholizadeh [b], Nobuhiro Tsuji [b], Cemal Cem Tasan [a,*]

[a] Department of Materials Science and Engineering, Massachusetts Institute of Technology, Cambridge, MA02139, USA
[b] Department of Materials Science and Engineering, Kyoto University, Kyoto, Japan

ABSTRACT

In contrast with pseudo-elasticity, martensite induced by plastic straining is known to exhibit limited further transformability and reversibility. The mechanistic and atomistic nature of a face-centered cubic (FCC)-hexagonal close-packing (HCP)-FCC sequential martensitic transformation pathway is investigated. Both transformations exhibit in the plastic realm and contribute to the observed strain hardening. In-situ electron microscopy and synchrotron diffraction verify that the final FCC-phase demonstrates strain accommodation capability. The random emission of Shockley partials in the HCP-martensite is identified as the most plausible atomistic mechanism for the second transformation, which renders a latent potential to dynamically mitigate stress concentration, enhancing strain hardenability.

© 2020 Acta Materialia Inc. Published by Elsevier Ltd. All rights reserved.

Introduction

Development of the physical understanding of mechanically-induced martensitic transformations (MT) and identification of the underlying atomistic mechanisms are of fundamental importance in the design of metallic and non-metallic materials [1–6]. Depending on the yield strength of the parent phase and thermodynamic driving force, this first-order diffusionless phase transformation can be realized with the assistance of elastic stress [7,8] or upon plastic straining [9,10]. In the former case, the resultant martensite has been well-documented to potentially enable pseudo-elastic or thermoelastic characteristics. That is, the removal of the external load, or imposition of heat, can reversely convert its crystallographic structure back to its parent phase [11,12]. In the latter case, however, martensite nucleation is usually accompanied by the introduction of an extensive defect density and significant plastic accommodation in its vicinity, resulting in mechanical irreversibility and limited further deformability [13–15]. A somewhat mixed scenario occurs when martensite with hexagonal close packing (HCP) structure is transformed from a face-centered cubic (FCC)-structured parent phase. The similar stacking sequence between FCC and HCP lattices renders milder plastic accommodation and thereby higher interfacial mobility [16–18]. Various electron microscopy studies of mechanically-metastable ferrous alloys have validated that this characteristic can consequently assist the incipience of a follow-up HCP to body-centered tetragonal (BCT) transformation by atomic shuffle [19–22]. From a broader perspective, HCP-structured phases have also been proved to demonstrate a displacive HCP→FCC transformation, especially under severe plastic deformation [23–27] or once their dimension can be reduced below a certain length-scale [22,28–31]. These observations initiate a fundamental proposition: is it possible to achieve an FCC→HCP→FCC sequential MT, in a single, bulk material, within one consistent plastic deformation process, such that strain hardening contributions due to MT can be enhanced? A recent *in-situ* transmission electron microscopy (TEM) study demonstrates the possibility for this transformation in thin foils [29]. In the present work, we provide experimental evidence for this unique MT pathway in a bulk alloy, demonstrate the associated strain accommodation process, and propose an atomistic mechanism that can realize this transformation.

An Fe-35Mn-10Co-10Cr (at.%) alloy was fabricated from vacuum induction melting [6,32], and its undeformed microstructure is presented in supplementary Fig. S1. *Ex-situ* uniaxial tensile testing reveals a yield strength of ~155 MPa and a significant strain hardenability, leading to an ultimate tensile strength of ~568 MPa and a fracture elongation of ~51% (Supplementary Fig. S1). *In-situ* tensile testing on specimens with applied speckle patterns [33] was performed on a Deben stage ($\dot{\varepsilon} = 10^{-4} \text{s}^{-1}$) inside a TESCAN MIRA 3 scanning electron microscope (SEM) equipped with electron backscatter diffractometer (EBSD). *In-situ* synchrotron X-ray diffraction experiments were carried out at the European Synchrotron Radiation Facility (beamline ID22, $\lambda = 0.1909$ Å, $\dot{\varepsilon} = 10^{-4} \text{s}^{-1}$). Diffrac-
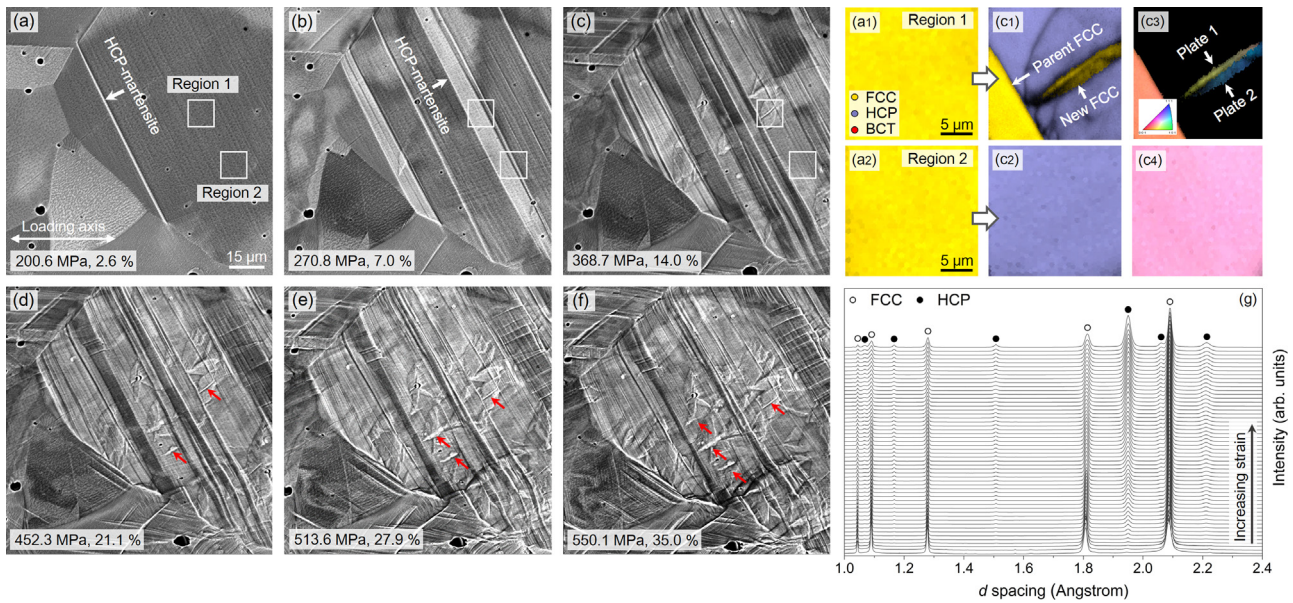
Fig. 1. *In-situ* observation of sequential FCC→HCP→FCC MT. (a)-(f) SEM micrographs for microstructural evolution at increasing deformation levels; (a1), (a2), (c1), and (c2) EBSD phase maps for Regions 1 and 2; (c3) and (c4) the corresponding IPFs; (g) synchrotron X-ray diffractograms taken with 1% engineering strain increments. To ensure clarity, high-magnification EBSD phase maps and inverse pole figures (IPF) are presented for two specific areas denoted as "Regions 1 and 2″ in (a).

tion patterns averaged from 20 scans (exposure time: 0.04 s) were recorded every 1% engineering strain until fracture, and were post-analyzed with the MAUD software [34] to accomplish Rietveld refinement.

In-situ BSE/EBSD micrographs in Fig. 1(a)–(f) reveal the phase constitution evolution with increasing deformation level. At a global stress of 200.6 MPa, the monitored microstructure undergoes a strain-induced FCC→HCP MT, resulting in a brighter orientation contrast (Fig. 1(a)). Upon further straining, both Regions 1 and 2 witness the same type of MT, forming a ~10 μm width HCP-martensite band (Fig. 1(b)). As global stress increases up to 368.7 MPa, these two regions demonstrate different micro-events: a spindle-shaped topography appears in Region 1, proved by EBSD phase map (Fig. 1(c1)), exhibiting an FCC structure, while HCP-martensite in Region 2 only thickens. This sort of clear distinctions in phase constitution evolution confirm that apart from the conventional FCC→HCP MT, a follow-up HCP→FCC MT is also activated in the present alloy, realizing a sequential FCC→HCP→FCC MT. Note the fact that the specimen is being constantly deformed in the plastic regime and the differences in crystallographic orientation between the newly formed FCC-phase and its parent counterpart (Fig. 1(c3)) clearly distinguish the sequential MT from classical stress-assisted reversible MT documented in pseudo-elastic materials, where the removal of external load is indispensable [8,35,36]. Upon elevating the global stress levels further (Fig. 1(d)–(f)), the sequential MT is also observed at multiple sites within the prior HCP-martensite bands (red arrows), during which no cracking presents, eliminating the potential interference from local unloading.

To further validate that this unique MT pathway does not involve any potential intermediate state [21,22], tensile experiments were also performed under synchrotron X-ray radiation. Diffractograms in Fig. 1(g) reveal that in the undeformed state, the examined alloy consists of a major FCC-phase (~98%) and minor amounts of thermally-induced HCP-phase (~2%). Lattice constants for FCC and HCP-phases are determined as a_{FCC} = 3.6140 Å (undeformed), a_{HCP} = 2.5524 Å, c_{HCP} = 4.1445 Å (~1% strain). When applied stress increases, characteristic diffraction peaks for the HCP-phase arise and their intensities witness an increasing trend un-

til fracture. Throughout the whole testing realm, neither additional peaks corresponding to a transitional structure nor FCC peak splitting is detected. These results are consistent with the *in-situ* SEM/EBSD observations, suggesting that the sequential MT is realized without the aid of any intermediate phase, and that the end product preserves the symmetry of the parent FCC-phase, but exhibiting a different crystallographic orientation (Fig. 1(c3)), more detailed crystallographic characterizations are shown in supplementary Fig. S2).

Assessments of phase fraction evolution analyzed from *in-situ* synchrotron diffraction and SEM/EBSD experiments are shown comparatively in Fig. 2. In both cases, the HCP-phase fraction reveals a monotonic increasing trend with the elevating applied stress. Unlike previous experimental observations [1,37–40] and theoretical predictions [41–43] of strain-induced martensite formation kinetics in classical metastable alloys, synchrotron X-ray diffractograms reveal a clear inflection at a stress level of ~220 MPa in the HCP-phase fraction evolution curve followed by a plateau-like region terminating at ~300 MPa (Fig. 2(a)). The most plausible reason for such a momentarily stunted FCC→HCP transformation rate is that the formation of new FCC-phases exhibits a burst-type of nucleation but negligible growth kinetics. This says, at a certain applied stress level, large amounts of new FCC-phases will abruptly nucleate due to the HCP→FCC MT, which would, as a net result, mitigate the nominal HCP-phase fraction increase. Because of the strong mechanical confinement from the adjacent prior HCP-martensite (Fig. 1(c)), these newly formed FCC-phases can scarcely thicken, and upon the consumption of all potential nucleation sites, their total fraction will reach to a stable value, resulting in the expedited increase of nominal HCP-phase fraction. Microstructure-based phase fraction analysis (Fig. 2(b)) also confirms that the FCC-phase resulting from the sequential MT, although low in amount, indeed exhibits an incremental growth in its fraction until necking or macroscopic failure terminates the deformation. Note that this kind of almost linearly increasing new FCC-phase fraction seen in Fig. 2(b) is mostly ascribed to the fact that the corresponding nucleation procedure has not exceeded its saturation state before the incipience of plastic instability. To explore whether this sequential MT can be activated to realize even higher FCC-phase fraction
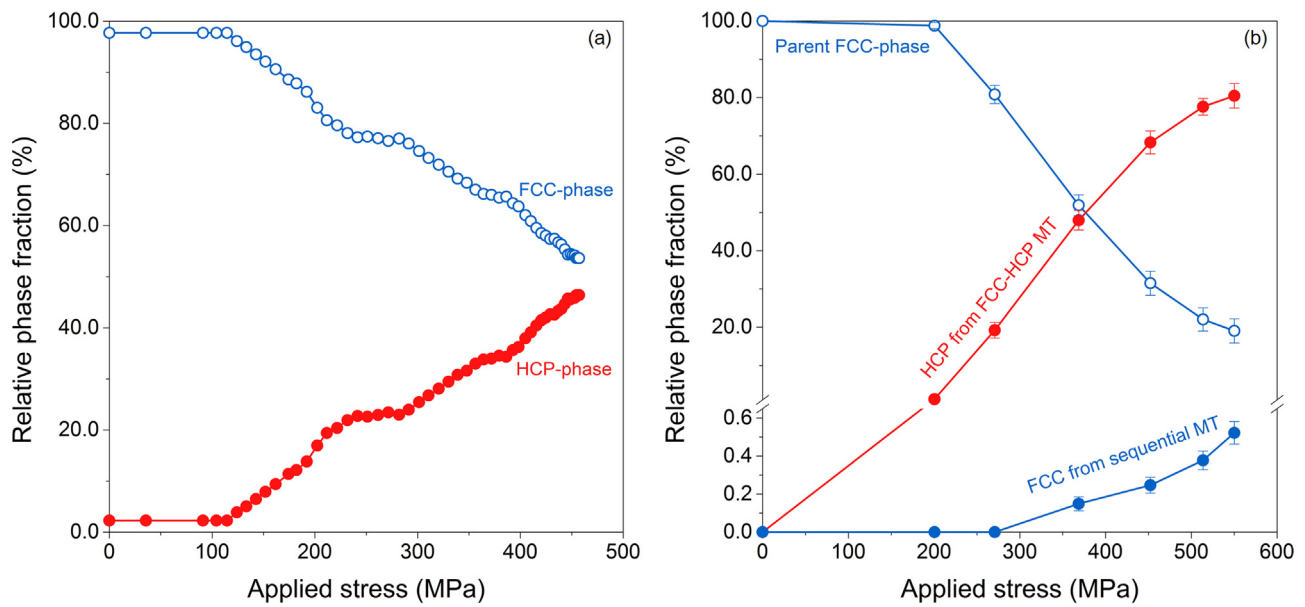
Fig. 2. Phase constitution evolution as a function of increasing applied stress analyzed from synchrotron X-ray diffractograms (a) and SEM/EBSD results (b).
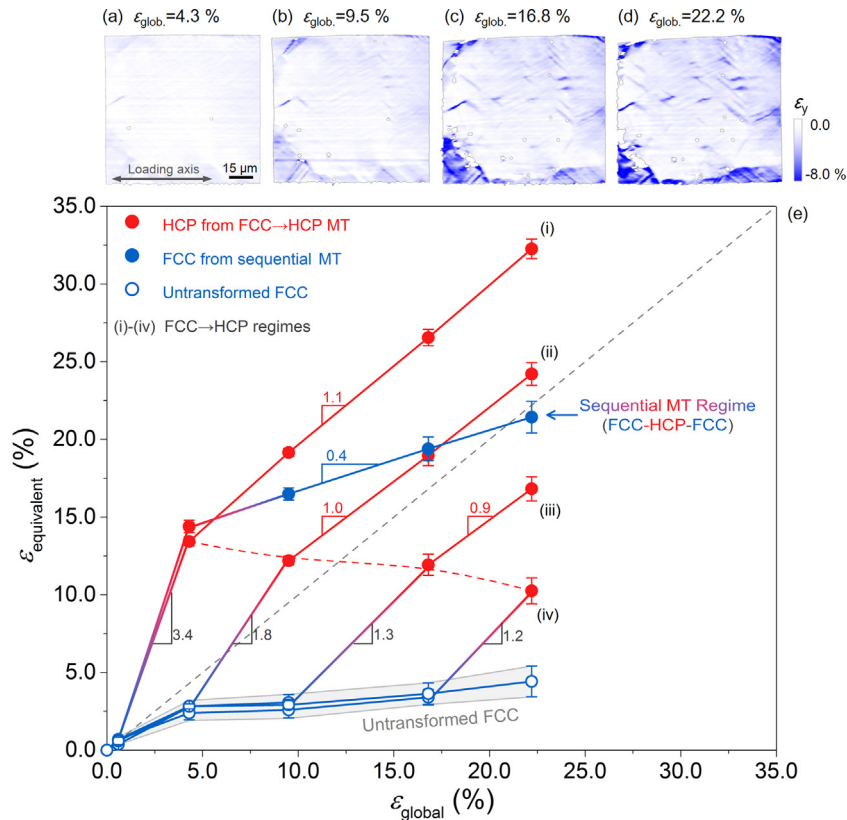

Fig. 3. Microstructure-based strain evolution assessment. (a)–(d) transverse component of the two-dimensional strain field calculated from displacement correlation algorithm; (e) site-specific local von Mises strain evolution with respect to increasing global strain level. The corresponding two-dimensional von Mises equivalent strain maps are provided in supplementary (Fig. S4 (a1)–(a4)).

when plastic instability can be delayed or even prohibited, we have carried out a separate set of high-pressure torsion experiments where larger amounts of shear deformation can be imposed on the specimens. BSE micrographs [supplementary Fig. S3] acquired at a local equivalent strain level of 42.5% (kept equal to the fracture true strain during uniaxial tensile deformation) confirms that the presence of larger amounts of new FCC-phase forming both within and at the junction of HCP-martensite bands.

Next, we focus on meso–scale strain evolution associated with the sequential MT. For clearer representations, only the transverse component (vertical to the loading axis) of the strain field (ε_y) is depicted in Fig. 3(a)–(d). As seen in the transverse strain maps where the global strain develops from 4.3 to 22.2% (Fig. 3(a)–(d)), regions where sequential MT is activated exhibit pronounced localized compressive strain: ε_y reaches −8.9% at 22.2% global strain (supplementary Fig. S4). In contrast, lower compressive strains

(−2.0~−3.0% in ε_y) are generated in the rest of the microstructure that only undergoes FCC→HCP MT. Such distinctions indicate an eminent difference in compressive strain accommodation between FCC→HCP and HCP→FCC MTs, again suggesting that the latter MT is not accomplished by replicating the strain trajectory of the former one in reverse. Atomistic mechanisms regarding this sequential MT will be elaborated in detail below.

Fig. 3(e) provides the calculated von Mises equivalent strain ($\varepsilon_{equivalent}$) evolution with respect to increasing global strain (ε_{global}) for all microstructural constituents, including (1) untransformed FCC-phase regions, (2) regions solely undergoing FCC→HCP MT, and (3) specific sites at which sequential MT takes place. Note that this plot should be distinguished from the classical strain partition assessment plots in which phase constitution change is typically not considered [44,45]. Due to the asynchronous activation of various plastic deformation modules, four specific regions (marked as (i)-(iv)) where FCC→HCP MT takes place successively at various ε_{global} levels are also presented to eliminate the interference from strain accommodation through perfect dislocation glide in the parent FCC-phase. At a global strain level of 4.3%, FCC→HCP MT is activated within Region (i), leading to a drastic $\varepsilon_{equivalent}$ increase to ~13.4%, suggesting the significant role of martensitic transformation strain in facilitating local plastic deformation. By comparing such transformation strains in Regions (i)–(iv), it can be concluded that although perfect dislocation glide-induced strain hardening in the parent FCC-phase imposes a slight suppression effect on transformation strain (the dashed red line and the indicated slope changes amongst (i)-(iv)), it is still the FCC→ HCP MT that acts as the major plastic strain carrier.

As global strain increases, the transformation product, HCP-martensite, subsequently reveals two kinds of local strain evolution characteristics depending on different deformation micro-events: (1) In some regions the HCP-martensite exhibits dislocation glide (portions extending further from the red dashed line). Here, the slopes witness a slight drop down to ~1.0 (compared to the slopes during FCC→ HCP MT), suggesting an enhanced plastic deformation resistance. Yet, within regions (i)–(iv), $\varepsilon_{equivalent}$ values yield a linear-like increasing trend as a function of elevating global strains. (2) In other regions, HCP→FCC MT takes place. Here, the most significant slope inflection from 3.4 to 0.4 is observed, and the corresponding $\varepsilon_{equivalent}$ also exhibits the most moderate monotonic increase. These distinctions highlight the following implications regarding the sequential MT: (1) the final transformation product, the FCC-phase, unlike typical BCT-phase that shows brittle-like characteristics [14,46], is able to realize further strain accommodation as deformation proceeds; (2) this sort of final FCC-phase possesses the most exceptional resistance to plastic deformation amongst all microstructural constituents, which is mostly ascribed to its extensive dislocation density [supplementary Fig. S3 (b)] inherited from two shear-dominant MTs; and (3) compared with the FCC→HCP MT, the sequential MT enables a more effective enhancement of local strain hardenability through the continuous formation of these highly-dislocated FCC-phases. We note that while these evidence all support the potential enhancement of strain hardenability, systematic measurement of phase stress together with load-sharing evolution still requires future effort to unambiguously evaluate the strain hardening contribution associated with the sequential MT.

2. Discussion

Atomistic mechanisms for FCC→HCP MT have been well-documented in the literature, following the classical Olson-Cohen partial dislocation emission model [47] in which the nucleation of HCP-martensite is accomplished through the mono-

directional gliding of $\frac{a}{6}\langle 112 \rangle_{FCC}$-type of Shockley partials on every other $\{111\}_{FCC}$ slip plane (Fig. 4(b) and (c)). This sort of mono-partial emission process results in triplex Burgers orientation relationships between HCP and FCC-phases: $\{111\}_{FCC}//\{0001\}_{HCP}$, $\langle 110 \rangle_{FCC}//\langle 11\bar{2}0 \rangle_{HCP}$, and $\langle 112 \rangle_{FCC}//\langle 10\bar{1}0 \rangle_{HCP}$. It could be hypothesized that by retracting the leading partials for them to re-associate with the trailing partials (or *vice versa*), the HCP→FCC MT can potentially be realized while simultaneously recovering the parent FCC-phase orientation (leading partials moving to trailing partials) or generating a $\Sigma 3$ boundary between them (trailing partials moving to leading partials). However, we argue that the sequential MT observed in the present study is not accomplished through this mono-partial emission scenario for the following reasons: (1) The IPF shown in Fig. 1(c3) reveals the distinctions in crystallographic orientation relationships between parent and newly formed FCC-phases, with no twin relation between them detected [supplementary Fig. S2 (f)]; (2) the meso–scale strain evolution chart demonstrates the HCP→FCC MT neither counteracts nor shows the identical transformation strain of its previous HCP→FCC MT; and (3) the sequential MT procedure takes place completely in the monotonic quasi-static plastic deformation realm where any re-occurrence of the parent phase at the bulk scale will violate the laws of energy dissipation [supplementary Fig. S5]. These observations, on the other hand, do imply it is the random partial emission (RPE) process [48,49] that assists the HCP→FCC MT. Such a mechanism involves synchronous activation of all possible partial dislocations, enabling stress delocalization while producing subtle macroscopic shape deformation in the parent phase, which is also rigidly in line with the much smaller $\varepsilon_{equivalent}$ increment with the HCP→FCC MT (Fig. 3(e)). As schematically illustrated in Fig. 4(e) and (f), by successively activating $\boldsymbol{b}_1$, $\boldsymbol{b}_2$, and $\boldsymbol{b}_3$ type of partials (Fig. 3(d)) on every other $\{0001\}_{HCP}$ plane, an FCC-structure can be consequently achieved, hence realizing the sequential FCC→HCP→FCC MT (energetic illustration is given in Supplementary Fig. S5).

The last point to address is whether or not this sequential MT demonstrates any latent capability to promote strain hardenability. To ensure better statistical assessment, the evolution of representative $(111)_{FCC}$ and $(222)_{FCC}$ lattice strains in the loading direction together with the corresponding stacking fault probability is presented in Fig. 4(a). As microscopic plastic incipience takes place (~120 MPa), both $(111)_{FCC}$ and $(222)_{FCC}$ planes reveal a significant relaxation in their lattice strains with monotonic incrementation in stacking fault probability, being recognized to potentially result from the nucleation of strain-induced HCP-martensite [50,52]. More surprisingly, the determined lattice strains undergo another relaxation at an applied stress level of ~300 MPa, upon which the stacking fault probability also reduces down to 0.0092, validating the annihilation of stacking faults during deformation. The atomistic mechanisms (Fig. 4(b)–(e)), the *in-situ* EBSD analyses (Fig. 1), and the phase constitution evolution (Fig. 2) discussed above all suggest that this phenomenon be mostly ascribed to the appearance of HCP→FCC transformation. Such a peculiar lattice strain relaxation along the loading direction (corresponds to the plateau in Fig. 2(a)) indicates that the sequential MT enables stress delocalization, promoting deformation homogenization. On the other hand, aside from the creation of extensive FCC/HCP boundaries that dynamically refine the prior HCP bands, a higher magnification EBSD micrograph confirms the presence of a unique $\Sigma 3$ boundary within the FCC-phase formed through the sequential MT (Supplementary Fig. S2). The formation of this sort of coherent boundary signifies the potential of strain hardenability promotion due to expedited dislocation multiplication and enhanced dislocation-boundary interaction [53]. It should be pointed out that whether this $\Sigma 3$ boundary forms following the classical mechani-
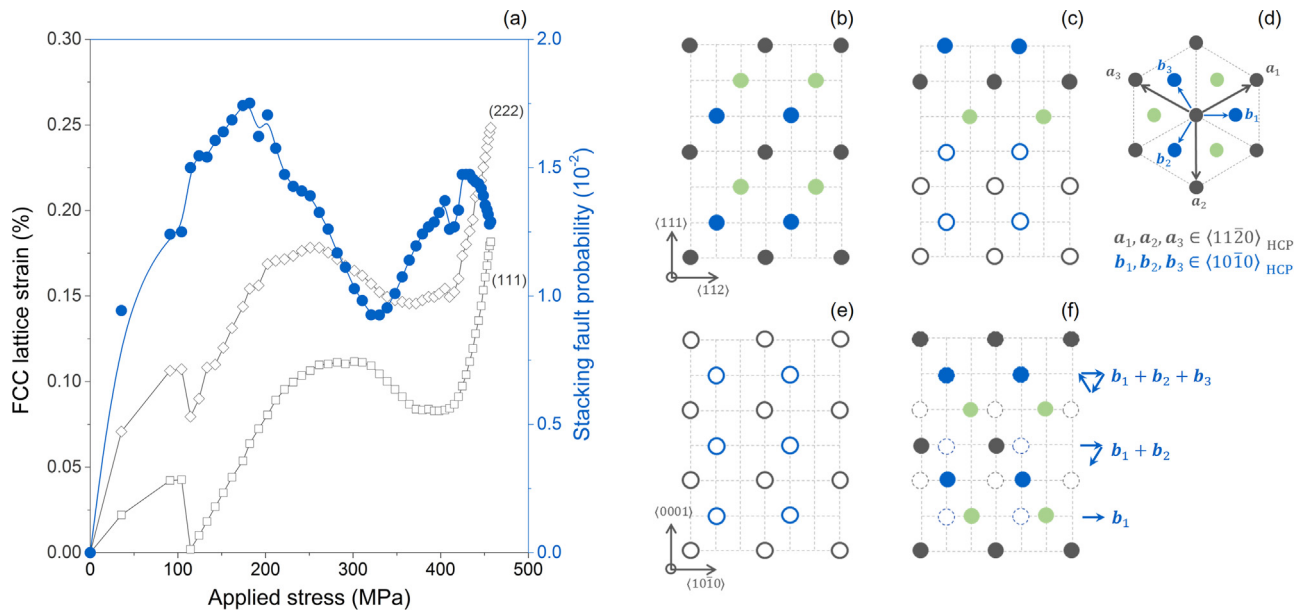
Fig. 4. Mechanisms for the sequential MT. (a) $(111)_{FCC}$ and $(222)_{FCC}$ lattice strains along the loading direction and the corresponding stacking fault probability (P_{sf}) determined using the effective $(111)_{FCC}$ and $(222)_{FCC}$ peak displacement through $P_{sf} = \frac{32\pi}{3\sqrt{3}}(\varepsilon_{222}^{eff} - \varepsilon_{111}^{eff})$ [50,51]; (b)–(f) atomistic configuration for mono-partial emission mechanisms accounting for FCC→HCP MT and random partial emission for HCP→FCC MT. Black, blue, and green represent A, B, and, C atomic layer while solid and haloed circles, respectively, denote FCC and HCP-phase. (For interpretation of the references to color in this figure legend, the reader is referred to the web version of this article.)

cal twinning mechanisms or *via* merging small lamellae of FCC that martensitically transform from different HCP basal planes, still requires further investigation.

In summary, we validated the presence of a unique FCC→HCP→FCC sequential MT at a bulk scale in the pure plastic deformation realm. We propose that this MT pathway is realized by random partial emission mechanisms, and that it not only leads to pronounced local compressive effect, but also results in significant lattice strain relaxation. Furthermore, meso–scale strain evolution and detailed electron microscopy studies suggest that although the resultant FCC-phase exhibits extensive dislocation density, it still accommodates plastic strain as deformation proceeds. These observations prove that the sequential MT enables both continuous stress delocalization and dynamic enhancement of plastic deformation resistance, indicating a latent strain hardenability. This sequential MT can be potentially achieved in other Mn-containing ferrous alloys or transformation-induced plasticity steels, opening a new route for advancing the fundamentals of MT and realizing more desirable mechanical performances.

Declaration of Competing Interest

The authors declare that they have no known competing financial interests or personal relationships that could have appeared to influence the work reported in this paper.

Acknowledgments

Supplementary materials

Supplementary material associated with this article can be found, in the online version, at doi:10.1016/j.scriptamat.2020.03.060.

References

[1] G.B. Olson, M. Cohen, Metall. Trans. A 6 (1975) 791–795.
[2] R.C. Garvie, R.H. Hannink, R.T. Pascoe, Nature 258 (1975) 703–704.
[3] A. Ferrari, D.G. Sangiovanni, J. Rogal, R. Drautz, Phys. Rev. B 99 (2019) 1–6.
[4] H. Huang, Y. Wu, J. He, H. Wang, X. Liu, K. An, W. Wu, Z. Lu, Adv. Mater. 29 (2017) 1–7.
[5] Y.I. Chumlyakov, I.V. Kireeva, O.A. Kutz, A.S. Turabi, H.E. Karaca, I. Karaman, Scr. Mater. (2016).
[6] S. Wei, J. Kim, C.C. Tasan, Acta Mater. 168 (2019) 76–86.
[7] A. Zangwill, R. Bruinsma, Phys. Rev. Lett. 53 (1984) 1073–1076.
[8] I. Müller, H. Xu, Acta Metall. Mater. 39 (1991) 263–271.
[9] G.B. Olson, M. Cohen, J. Less-Common Met. 28 (1972) 107–118.
[10] D.W. Suh, S.J. Kim, Scr. Mater. (2017).
[11] I. Karaman, B. Basaran, H.E. Karaca, A.I. Karsilayan, Y.I. Chumlyakov, Appl. Phys. Lett. 90 (2007) 1–4.
[12] Y. Yamada, Phys. Rev. B 46 (1992) 5906–5911.
[13] G.K. Tirumalasetty, M.A. Van Huis, C. Kwakernaak, J. Sietsma, W.G. Sloof, H.W. Zandbergen, Acta Mater. 60 (2012) 1311–1321.
[14] J. Liu, C. Chen, Q. Feng, X. Fang, H. Wang, F. Liu, J. Lu, D. Raabe, Mater. Sci. Eng. A 703 (2017) 236–243.
[15] F. Lani, Q. Furnémont, T. Van Rompaey, F. Delannay, P.J. Jacques, T. Pardoen, Acta Mater. 55 (2007) 3695–3705.
[16] O. Blaschko, G. Krexner, J. Pleschiutschnig, G. Ernst, C. Hitzenberger, H.P. Karnthaler, A. Korner, Phys. Rev. Lett. 60 (1988) 2800–2803.
[17] B.H. Jiang, T. Tadaki, H. Mori, T.Y. Hsu, Mater. Trans. JIM 38 (1997) 1078–1082.
[18] Y. Tomota, W. Nakagawara, K. Tsuzaki, T. Maki, Scr. Metall. Mater. 26 (1992) 1571–1574.
[19] X.S. Yang, S. Sun, H.H. Ruan, S.Q. Shi, T.Y. Zhang, Acta Mater. 136 (2017) 347–354.
[20] A. Sato, K. Soma, T. Mori, Acta Metall. 30 (1982) 1901–1907.
[21] H. Fujita, T. Katayama, Mater. Trans. 33 (1992) 243–252.
[22] K.H. Kwon, B.C. Suh, S. Il Baik, Y.W. Kim, J.K. Choi, N.J. Kim, Sci. Technol. Adv. Mater. 14 (2013).
[23] H. Shahmir, T.G. Langdon, Mater. Sci. Eng. A 704 (2017) 212–217.
[24] H. Zhao, X. Hu, M. Song, S. Ni, Scr. Mater. 132 (2017) 63–67.
[25] H.C. Wu, A. Kumar, J. Wang, X.F. Bi, C.N. Tomé, Z. Zhang, S.X. Mao, Sci. Rep. 6 (2016) 24370.

[26] H. Zhao, M. Song, S. Ni, S. Shao, J. Wang, X. Liao, Acta Mater. 131 (2017) 271–279.
[27] J.X. Yang, H.L. Zhao, H.R. Gong, M. Song, Q.Q. Ren, Sci. Rep. 8 (2018) 1992.
[28] Q. Yu, J. Kacher, C. Gammer, R. Traylor, A. Samanta, Z. Yang, A.M. Minor, Scr. Mater. 140 (2017) 9–12.
[29] W. Lu, C.H. Liebscher, G. Dehm, D. Raabe, Z. Li, Adv. Mater. 30 (2018) 1–10.
[30] J.Y. Li, W. Li, M.J. Jin, X.J. Jin, Mater. Res. Lett. 3 (2015) 107–113.
[31] W.Y. Wang, B. Tang, S.L. Shang, J. Wang, S. Li, Y. Wang, J. Zhu, S. Wei, J. Wang, K.A. Darling, S.N. Mathaudhu, Y. Wang, Y. Ren, X.D. Hui, L.J. Kecskes, J. Li, Z.K. Liu, Acta Mater. (2019).
[32] S. Wei, M. Jiang, C.C. Tasan, Metall. Mater. Trans. A Phys. Metall. Mater. Sci. 50 (2019) 3985–3991.
[33] D. Yan, C.C. Tasan, D. Raabe, Acta Mater. 96 (2015) 399–409.
[34] L. Lutterotti, Nucl. Inst. Methods Phys. Res. Sect. B Beam Interact. Mater. Atoms 268 (2010) 334–340.
[35] Z. Zhang, X. Ding, J. Sun, T. Suzuki, T. Lookman, K. Otsuka, X. Ren, Phys. Rev. Lett. 111 (2013) 145701.
[36] N. Abdolrahim, I.N. Mastorakos, H.M. Zbib, Phys. Rev. B - Condens. Matter Mater. Phys. 81 (2010) 1–5.
[37] P. Schloth, M.A. Weisser, H. Van Swygenhoven, S. Van Petegem, P. Susila, V. Subramanya Sarma, B.S. Murty, S. Lauterbach, M. Heilmaier, Scr. Mater. 66 (2012) 690–693.
[38] Y. Tian, S. Lin, J.Y.P. Ko, U. Lienert, A. Borgenstam, P. Hedström, Mater. Sci. Eng. A 734 (2018) 281–290.
[39] S. Harjo, N. Tsuchida, J. Abe, W. Gong, Sci. Rep. 7 (2017) 2–4.
[40] R. Blondé, E. Jimenez-Melero, L. Zhao, J.P. Wright, E. Brück, S. van der Zwaag, N.H. van Dijk, Mater. Sci. Eng. A 618 (2014) 280–287.
[41] R.G. Stringfellow, D.M. Parks, G.B. Olson, Acta Metall. Mater. 40 (1992) 1703–1716.
[42] T. Park, L.G. Hector, X. Hu, F. Abu-Farha, M.R. Fellinger, H. Kim, R. Esmaeilpour, F. Pourboghrat, Int. J. Plast. 120 (2019) 1–46.
[43] M. Zecevic, M.V. Upadhyay, E. Polatidis, T. Panzner, H. Van Swygenhoven, M. Knezevic, Acta Mater. 166 (2019) 386–401.
[44] S. Hémery, P. Villechaise, Acta Mater. 171 (2019) 261–274.
[45] A. Fillafer, C. Krempaszky, E. Werner, Mater. Sci. Eng. A 614 (2014) 180–192.
[46] J.W. Christian, Mater. Trans. JIM 33 (1992) 208–214.
[47] G.B. Olson, M. Cohen, Metall. Trans. A 7 (1976) 1897–1904.
[48] X.L. Wu, X.Z. Liao, S.G. Srinivasan, F. Zhou, E.J. Lavernia, R.Z. Valiev, Y.T. Zhu, Phys. Rev. Lett. 100 (2008) 5–8.
[49] B.Q. Li, B. Li, Y.B. Wang, M.L. Sui, E. Ma, Scr. Mater. 64 (2011) 852–855.
[50] J.S. Jeong, W. Woo, K.H. Oh, S.K. Kwon, Y.M. Koo, Acta Mater. 60 (2012) 2290–2299.
[51] R.P. Reed, R.E. Schramm, J. Appl. Phys. 45 (1974) 4705–4711.
[52] S.F. Liu, Y. Wu, H.T. Wang, W.T. Lin, Y.Y. Shang, J.B. Liu, K. An, X.J. Liu, H. Wang, Z.P. Lu, J. Alloys Compd. 792 (2019) 444–455.
[53] L. Zhu, H. Ruan, X. Li, M. Dao, H. Gao, J. Lu, Acta Mater. 59 (2011) 5544–5557.